atmosphere

MDPI

Article

Multi-Sensor Instrument for Aerosol In Situ Measurements

Ilya Bruchkouski, Artur Szkop *, Jakub Wink, Justyna Szymkowska and Aleksander Pietruczuk

Institute of Geophysics Polish Academy of Sciences (IGF PAN), 01-452 Warszawa, Poland; ibruchkouski@igf.edu.pl (I.B.); jakubw@igf.edu.pl (J.W.); jszymkowska@igf.edu.pl (J.S.); alek@igf.edu.pl (A.P.)
* Correspondence: aszkop@igf.edu.pl

Abstract: A short comparison campaign took place at the Racibórz measurement site in May 2024 to assess the consistency of the Integrated Aerosol Monitoring Unit (IAMU), which houses three PM aerosol sensors (SPS30, OPC-N3, and OPS 3330) within a single enclosure. This assessment was supported by simultaneous measurements from two reference instruments (APS 3321 and SMP S3082), along with auxiliary observations from a ceilometer and meteorological station. To enhance particle transmission efficiency to the IAMU sensors, aerodynamic modeling of the inlet pipes was performed, accounting for particle density and diameter. The primary objective of this study was to evaluate the feasibility of using the IAMU, in conjunction with optimized inlet designs, for PM monitoring under varying ambient relative humidity and sensor temperature conditions. IAMU measurements have shown large absolute differences in PM values (exceeding one order of magnitude) with moderate (>0.54 for PM_{10}) to high (>0.82 for $PM_{2.5}$ and PM_1) temporal correlations. A calibration method was proposed, using reference instrument data and incorporating sensor temperature and air sample humidity information. The IAMU, combined with the developed calibration methodology, enabled the estimation of the aerosol growth factor, deliquescence point (RH ≈ 65%), and PM_1 hygroscopic parameter κ (0.27–0.56) for an industrial region in Poland.

Keywords: aerosol size distribution; aerosol in situ measurements; SPS30; OPC-N3; OPS 3330; APS 3321; SMPS 3082; hygroscopic growth

Academic Editor: Kumar Vikrant

Received: 29 November 2024
Revised: 19 December 2024
Accepted: 24 December 2024
Published: 2 January 2025

Citation: Bruchkouski, I.; Szkop, A.; Wink, J.; Szymkowska, J.; Pietruczuk, A. Multi-Sensor Instrument for Aerosol In Situ Measurements. *Atmosphere* **2025**, *16*, 42. https://doi.org/10.3390/atmos16010042

1. Introduction

Measuring the size distribution of aerosol particles plays a key role in air quality monitoring, as aerosols have a significant impact on human health, climate, and the environment [1]. The mass of a given aerosol fraction is often described as PM_x, which stands for micrograms of particulate matter with aerodynamic diameters smaller than x micrometers suspended in a cubic meter of air. Aerosol particles, particularly those in the fine ($PM_{2.5}$) and ultrafine ($PM_{0.1}$) size ranges, pose serious health risks. These particles can penetrate deep into the respiratory system, leading to cardiovascular and respiratory diseases and, in some cases, premature death [2]. Fine and ultrafine particles are also known to cause inflammation and oxidative stress in the lungs and bloodstream, increasing the risk of chronic diseases like asthma, lung cancer, and heart disease [3,4].

Aerosol particles influence the Earth's climate in two primary ways: by directly scattering and absorbing solar radiation (direct effect) and by acting as cloud condensation nuclei (CCN) and ice-nucleating particles (INP), which modify cloud properties (indirect effect) [5]. This alters the Earth's radiation balance, affecting global and regional climate systems. For example, sulfates and other fine aerosols have a cooling effect by reflecting

sunlight, while black carbon (soot) absorbs heat, contributing to warming [6]; therefore, aerosol size distribution and its composition is crucial to understanding radiative forcing.

Traditionally, expensive, stationary measuring instruments with high accuracy and the ability to provide detailed data on particle sizes and concentrations have been used for this purpose. Table 1 presents the main types of commonly used high-precision stationary instruments for aerosol size distribution measurements.

Table 1. Overview of instruments for aerosol size distribution measurements.

Instrument	Approximate Size Range (μm)	Principle	Measured Quantity
NAIS Neutral Cluster and Air Ion Spectrometer	0.002–0.04	Electrical mobility + Electrometer	Stokes diameter
MPSS Mobility Particle Size Spectrometer	0.01–0.8	Electrical mobility + Condensation Particle Counter	Stokes diameter
APSS Aerodynamic Particle Size Spectrometer	0.5–20	Aerodynamic sizing	Aerodynamic diameter
OPSS Optical Particle Size Spectrometer	0.3–10	Wide-angle light scattering	Optical diameter
OPC Optical Particle Counter	0.3–10	Narrow angle light side-scattering	PM_1, $PM_{2.5}$, PM_{10} (based on optical scattering)
Cascade Impactor	0.01–100	Aerodynamic separation through impaction	Aerodynamic diameter

However, the high cost and bulkiness of such systems limit their use, especially in conditions requiring the deployment of multiple measurement points or mobile monitoring. In this regard, there is a need to develop and test more affordable and compact solutions that still can provide high-quality data.

This paper considers an approach based on the use of a combination of three different aerosol sensors placed in a single housing as the Integrated Aerosol Monitoring Unit (IAMU). Two of these sensors, the SPS30 (Sensirion Europe GmbH, Gerlingen, Germany) and OPC-N3 (Alphasense AMETEK, Braintree, United Kingdom), are low-cost, compact sensors intended for mass use. The third sensor, the OPS 3330 (TSI GmbH, Aachen, Germany), is a more advanced instrument capable of measuring particle size distribution with high accuracy. The main objective is to test the possibility of using the IAMU for air quality monitoring, as well as to evaluate its performance in comparison with high-precision equipment at different air sample humidities and different IAMU temperatures. Due to the significant difference in the heat capacity of air and the contents of the IAMU enclosure, the embedded temperature detector in this case will measure the temperature of the OPS-N3 itself. Assuming a uniform temperature distribution inside the IAMU enclosure, we will further assume that temperature data obtained by the OPS-N3 sensor are used as the temperature of all IAMU sensors.

To ensure correct air sampling, sampling tubes were modelled and manufactured for each of the sensors, considering the aerodynamic parameters of air, the performance of the sensor pumps and the microphysical characteristics of various aerosol fractions. The introduction of this approach could significantly expand the capabilities of air quality monitoring, making it more accessible and flexible for widespread use.

During the study, the IAMU was installed at the Racibórz measurement site together with stationary aerosol measuring instruments (APS 3321 and SMPS 3082, TSI GmbH, Aachen, Germany). Measurements took place during the period of 6 May 2024 to 13 May 2024, which allowed for a direct comparison between the data series and for conclusions to be drawn about the suitability of using inexpensive sensors in real conditions.

2. Materials and Methods

2.1. Aerodynamic Modeling for the Inlet Pipe

To accurately simulate the air intake process through the inlet pipe, it was necessary to measure the pump performance of each instrument, which was done by the TSI 41401 (TSI GmbH, Aachen, Germany) flow meter. The measured pump performance was 0.125, 0.50, and 1.00 L/min for the SPS30, OPC-N3, and OPS 3330, respectively. Aiming to maximize the number of particles entering the sensors, the optimization of the configuration of the sampling pipes for the aerosol sensors was carried out. The model study, performed in SOLIDWORKS Flow Simulation [7], utilized eleven aerosol fractions with different particle diameter sizes: 0.2, 1.0, 2.0, 3.0, 4.0, 5.0, 6.0, 7.0, 8.0, 9.0 and 10.0 μm, with densities of 1.7 g/cm^3 [8]. The following parameters and conditions were considered:

- Orientation of tubes in the gravitational field: vertically oriented intake pipes require protection against rain; therefore, the air sample should be drawn from the bottom. In this configuration, gravitational force tends to remove heavy particles from the flow, making it necessary to maintain a certain air velocity near the air sampling pipe for accurate sampling.
- Model of particle adhesion to the walls: we assumed complete adhesion of particles to the inner walls of the pipes. This means that if a particle touches the wall, it will no longer be involved in the air motion, allowing us to consider particle losses on the walls.
- Flow instability: non-stationary aspects of the flow, including turbulent effects, were considered to achieve a more accurate description of particle motion within the pipes.
- Tube wall roughness: the modeling accounted for a pipe inner wall roughness of 2 μm, which influenced both the flow dynamics and particle–surface interactions by affecting the air velocity distribution inside the pipe.
- Boundary conditions: atmospheric pressure (101,325 Pa), temperature (20 °C), relative humidity (50%), and pump performances (1 L/min, 0.5 L/min and 0.125 L/min) were used as initial operating conditions.
- Horizontal wind speed: the horizontal wind speed was varied from 0 to 10 m/s in 1 m/s increments, enabling the assessment of external conditions on particle capture efficiency.

The air flow modeling, together with eleven aerosol fractions, was performed using computational fluid dynamics (CFD) methods within the Flow Simulation environment as an internal problem with corresponding boundary conditions at two cross-sections of the inlet pipe. More than 20 cases of the geometry of the sampling pipe for the specified aerosol fractions were investigated. For each case, the fraction of particles that entered the corresponding aerosol measurement instrument was compared with number of particles in the vicinity of the horizontal cross-section of the inlet pipe.

The geometry parameters of the model for which changes were considered were the shape of the air-conducting channel and its size in different cross-sections of the inlet pipe. Next, for the existing model, an aerodynamic calculation and a calculation of particle motion were launched, taking into account the initial and boundary conditions. The percentage of particles of all fractions that reached the end of the pipe (sensor) served as the criteria for the success of the calculation.

Figure 1a shows the sampling pipe shape in cross-section during the modeling process; the final geometry of the sampling tube with dimensions is presented in Figure 1b, and Figure 1c shows a CAD model with necessary joints.

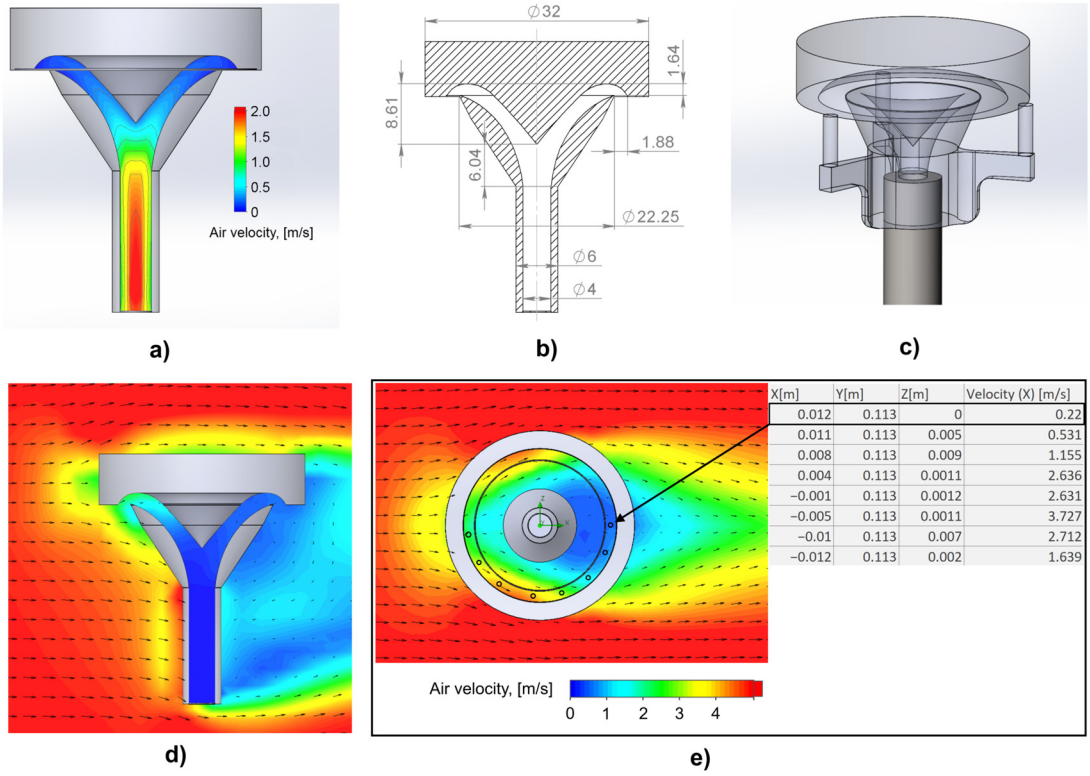

Figure 1. Modeled air velocity distribution in the sampling head (**a**); main dimensions in mm (**b**); CAD model of inlet pipe configuration (**c**); modeled field of horizontal air velocity (**d**); and cross-sectional view (A-A) of horizontal velocity field near the inlet (**e**).

In real-world in situ measurements, there is almost always some wind, and the air velocity distribution in the vicinity of the inlet pipe will not be homogeneous as shown at Figure 1d. Therefore, to more accurately determine the boundary conditions for the internal problem-solving, depending on the wind velocity data from the nearby weather station, it is necessary to obtain the air velocity distribution in the vicinity of the inlet pipe.

After determining the optimized configuration of the cross-section of the inlet pipe, which can allow for obtaining good aerosol particle transmission for all fractions, the efficiency coefficient $k(v_x)$ of the inlet pipe, depending on the horizontal air velocity v_x, was calculated. In this case, the external problem was considered in terms of vector field of air velocity distribution in some volume around the inlet pipe. For the internal problem, the parameters of the moving medium were consistent: air at atmospheric pressure (101,325 Pa), a temperature of 20 °C, a relative humidity of 50%, and an internal wall roughness of 2 µm. Consequently, the external problem was analyzed for varying medium velocities while preserving the same object.

In Figure 1d,e, the vector field of air velocity distribution is shown as an example of the modeling results for horizontal air velocity 5 m/s is presented.

The average velocity obtained from the external problem for a given horizontal wind velocity was used. As an example, in Figure 1e, 8 points of interest at the cross-section are shown and corresponding horizontal velocity components are determined for each point of interest. Thus, for each point of interest, the velocity coefficients are determined and the average horizontal component in the vicinity of the inlet for a given horizontal wind is calculated.

As a result, the measurement model can be described as follows:

- Wind parameters measurements and horizontal wind speed calculation:

$$\vec{V}_{hor} = \vec{V}_x + \vec{V}_y \quad (1)$$

- Calculation of the average horizontal velocity component in the vicinity of the inlet $v_x = a \cdot |\vec{V}_{hor}|$, where a—Calculated velocity coefficients;
- Determination of the pipe efficiency coefficient $k(v_x)$ based on the solved internal problem for different v_x as the boundary conditions;
- Aerosol number concentrations are calculated by formula:

$$A = \frac{A_{measured}}{k(v_x) \cdot H(d)} \quad (2)$$

where A—Corrected aerosol number concentration;

$A_{measured}$—Measured aerosol number concentration by the instrument;
$k(v_x)$—Pipe efficiency coefficient, which is dependent on average wind velocity v_x;
v_x—Average horizontal wind velocity in the vicinity of the inlet;
$H(d)$—Calibration coefficient of the instrument.

2.2. Instrumentation

The following sensors were used as compact, inexpensive measuring instruments: the SPS30 and Alphasense OPC-N3. According to its specification, SPS30 is able to measure number concentrations $PM_{0.5}$, $PM_{1.0}$, $PM_{2.5}$, PM_4, and PM_{10} with a sampling interval of 1 s; OPC-N3 is able to detect particles from 0.35 µm to 40 µm in diameter with 24 bins and convert measurements into mass concentrations of $PM_{1.0}$, $PM_{2.5}$, and PM_{10} using embedded algorithms. To validate the performance of these low-cost detectors, we included the TSI OPS 3330 as a reference instrument in the enclosure. All sensors were installed in a common enclosure, with a dedicated inlet pipe designed for each sensor. The dimensions of the enclosure itself are 580 × 430 × 230 mm, the weight of the IAMU is 10 kg without batteries, the height of the inlet pipes from the plane of the enclosure is 250 mm.

It should be noted that the SPS30 has two inlets, and, therefore, for its correct operation, it needs a connection unit, which will be able to connect the inlet pipe and sensor themselves. The SPS30 with the connection unit is shown in Figure 2a.

The measurement setup is illustrated in Figure 2b, which comprises two Raspberry Pi microcomputers (a Raspberry Pi 3B and a Raspberry Pi Zero W) equipped with sensors for particle detection: an OPC-N3 optical particle counter and an SPS30 suspended dust sensor, as schematically shown in Figure 2c. The system is powered by a 12 V 5 A supply, which is stepped down to 5 V using two DC/DC 12 V to 5 V converters to match the operating voltage of the microcomputers.

The Raspberry Pi 3B acts as the central controller for the system, providing processing and memory resources. It powers the OPC-N3 sensor and records its data at 1 s intervals. Additionally, it serves as a Wi-Fi access point, allowing remote devices to connect, download, and manage data. The Raspberry Pi 3B also receives and stores data sent from the Raspberry Pi Zero W, which operates in parallel.

The Raspberry Pi Zero W powers and collects data from the SPS30 sensor, which also measures particle concentrations every second. Every 5 min, the Raspberry Pi Zero W transmits the accumulated SPS30 data to the Raspberry Pi 3B for consolidated storage, making this setup a flexible, networked solution for high-frequency particulate matter measurement.

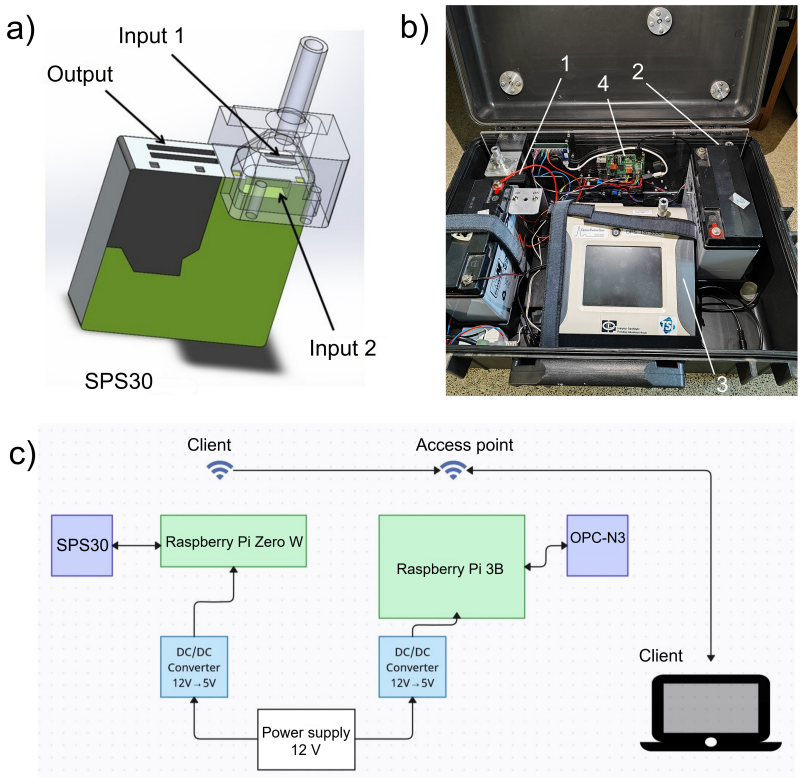

Figure 2. IAMU sensors: (**a**) CAD model of SPS30 sensor with connection unit (transparent); (**b**) Common enclosure view: 1—OPC-N3, 2—SPS30, 3—OPS3330, 4—Raspberry Pi 3B; (**c**) SPS30 and OPC-N3: Connection schematic and data transmission.

An SMPS 3082 (scanning mobility particle sizer) calculates particles' Stokes radius by measuring the speed at which ionized aerosol particles drift in an electric field. The instrument is comprised of three main components: an impactor that cuts off large aerosols, a differential mobility analyzer (DMA) that classifies the particles' mobility by discretely modifying the electric field, and a condensation particle counter (CPC) that uses supersaturated working fluid vapors to condense and grow particulates, allowing for their optical detection. Our TSI Model 3082 SMPS provides mobility aerosol size distribution in the 10–800 nm range.

In Figure 3, the external view of the IAMU, together with pipes for the stationary instruments SMPS 3082 and APS 3321 during the measurement campaign, is shown.

(**a**) (**b**)

Figure 3. Integrated Aerosol Monitoring Unit (IAMU) during comparison campaign in Racibórz: (**a**) IAMU; (**b**) Common view of IAMU together with pipes for stationary instruments SMPS3082 and APS3321.

An APS 3321 (aerodynamic particle sizer) uses a laser-based, dual-optical-axis detection method to measure individual particle's time-of-flight under aerodynamic acceleration in a laminar flow, as well as light-scattering intensity. The TSI Model 3321 APS can obtain aerodynamic particle size distribution in the 0.5–20 µm range with a resolution of 52 channels.

2.3. Data Processing

OPS 3330 can measure number count N_i in #/cm^3 at size channel i. For calculating volume concentration $\frac{dV}{dlogD_p}$ at each particle diameter bin, the following formula is used:

$$\frac{dV}{dlogD_p} = \frac{N(D_p)}{Q \cdot (t_s - t_d)} \cdot \frac{\pi}{6} \cdot D_p^3 \quad (3)$$

where

D_p—particle diameter at the midpoint of the bin (µm);
N_i—number count in #/cm^3 at size channel i;
Q—sample flow rate, 16.67 cm^3/s;
t_s—sample time (s);
t_d—dead time (s).

For data normalization, the logarithmic difference of the particle diameter bin edges is applied according to the formula:

$$\Delta logD_p = log_{10}(D_{p,\ i+1}) - log_{10}(D_{p,\ i}) \quad (4)$$

PM_x concentration refers to the particulate matter with an aerodynamic diameter, which is less than or equal to x µm, assuming a spherical shape for particles. For each bin with a diameter below x µm, the mass concentration in µg/m^3 of the total amount of particles is calculated by the formula [9–11]:

$$PM_x = \rho \cdot \sum_{D_p \leq x\ \mu m} \frac{dV}{dlogD_p} \cdot \Delta logD_p \quad (5)$$

where

PM_x—mass concentration for the specified size;
D_i—midpoint diameter of the particles at i-th bin,
ρ—particle density, assuming a standard density for ambient aerosols (e.g., ρ = 1.5 g/cm^3);
$\Delta logD_p$—difference in the logarithmic diameter of the bin edges.

To obtain a wide range particle size distribution from combined SMPS 3082 and APS 3321 in situ measurements, different working principles of the two instruments need to be considered. The SMPS 3082 measures mobility (Stokes) particle diameters, while the APS 3321 provides data on aerodynamic diameters. Assuming spherical particles, these two quantities are connected through the following equation [12]:

$$D_{Aerodynamic} = D_{Stokes} \sqrt{\frac{\rho_P}{\rho_0}} \quad (6)$$

where

$D_{Aerodynamic}$—particle aerodynamic diameter;
D_{Stokes}—particle mobility (Stokes) diameter;
ρ_P—relative particle mean density;
ρ_0—reference calibration particle density 1.0 g/cm^3.

Thus, the continuous aerodynamic particle number concentration $\frac{dN}{dlogD_p}$ can be calculated. Therefore,

$$\frac{dV}{dlogD_p} = \frac{dN}{dlogD_p} \cdot \frac{\pi}{6} \tag{7}$$

$$\Delta logD_p = log_{10}\left(\sqrt{d_i \cdot d_{i+1}}\right) - log_{10}\left(\sqrt{d_{i-1} \cdot d_i}\right) = Const \tag{8}$$

$$PM_x = \rho \cdot \Delta logD_p \sum_{D_p \leq x \text{ m}} \frac{dV}{dlogD_p} \tag{9}$$

where $\Delta logD_p$ is the logarithmic bin width, which is representing the bin boundaries and calculated from corresponding midpoints d_i.

3. Results

3.1. Size Distribution Based on the State-of-the-Art Instruments—The Benchmark

To characterize aerosol size distribution comprehensively across a broad diameter range (10 nm–10 µm), we employed a tandem of advanced aerosol size spectrometers. The aerosol samples were dried to a relative humidity (RH) below 40% with Nafion membrane dryers to effectively ensure that no hygroscopic growth occurred on the particles. These high-performance instruments provided detailed insights into both fine and coarse aerosol distributions, serving as a benchmark for comparative analysis.

The aerosol measurements were conducted assuming a standard mean density for fine aerosols, yielding data that, overall, aligned well with expected distributions, though occasional mismatches were noted. The size distribution data from the reference instruments allowed for the collection of cross-correlation with observations from a collocated vertical profiler (ceilometer), enabling an enriched understanding and better verification of aerosol dynamics.

An illustrative example is shown in Figure 4, highlighting a nocturnal residual layer that gradually descends, reaching the surface around 5:00 UTC.

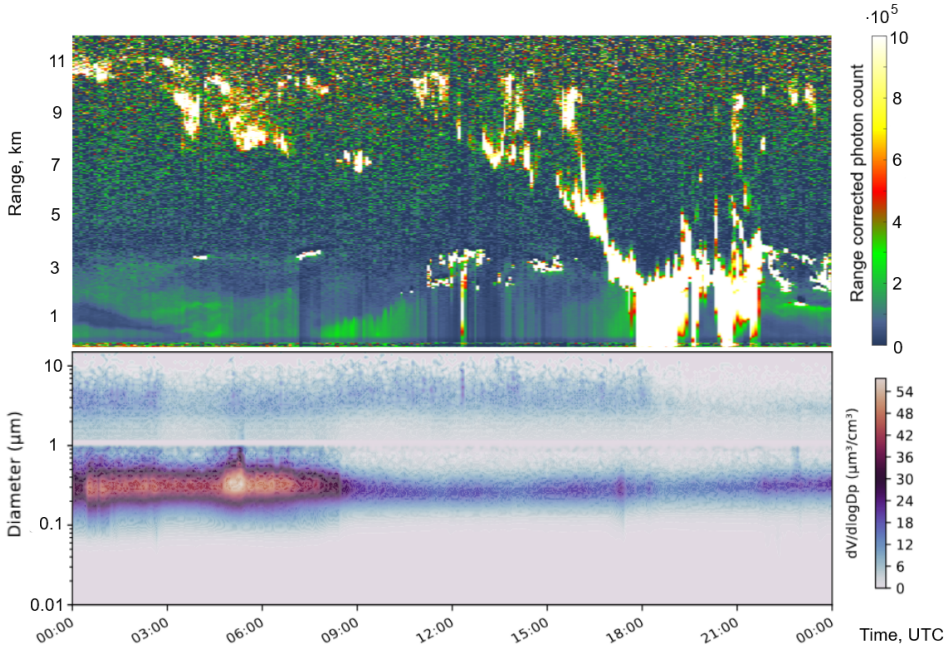

Figure 4. Racibórz, 5 May 2024: The upper panel displays ceilometer data (Lufft CHM15k Nimbus), while the lower panel presents the aerosol differential volume distribution $\frac{dV}{dlogD_p}$ measured by stationary instruments. The SMPS 3082 was used for particle diameters in the range of 0.01–1 µm and the APS 3321 for diameters ranging from 1 to 10 µm.

This descent is clearly identifiable in the size distribution data, evidenced by an increase in fine fraction concentrations as the layer approaches ground level. From Figure 4, it can be seen that, with the onset of daylight, the convective boundary layer begins to develop, lifting near-surface aerosols and causing a marked decrease in ground-level concentrations around 8:00 UTC. Later in the day, beginning at approximately 18:00 UTC, precipitation events detected in the ceilometer signal drive a wet deposition process, predominantly affecting the coarse aerosol fraction, evidenced by a sharp reduction in concentrations of large particles.

These observations demonstrate both gradual and rapid shifts in aerosol concentration levels, providing a reliable benchmark against which the performance and accuracy of low-cost sensors can be assessed.

3.2. Performance of Custom Intake Manifolds

The optimal geometry of the intake manifold was identified through an iterative optimization process that utilized computational fluid dynamics (CFD) simulations. This approach incorporated various aerosol types to enhance the transmission efficiency of aerosol particles under a broad spectrum of operating conditions.

During the optimization process, eleven distinct aerosol populations with aerodynamic diameters of 0.2, 1.0, 2.0, 3.0, 4.0, 5.0, 6.0, 7.0, 8.0, 9.0, and 10.0 µm and a uniform density of 1.7 g/cm^3 were evaluated. The design achieving the highest average transmission efficiency across these aerosol size distributions was selected as the final configuration.

The performance of the inlet pipe was assessed for the given eleven aerosol fractions under varying horizontal wind speeds (0 to 10 m/s) and at three pump flow rates (0.125, 0.5, and 1.0 L/min), as depicted in Figure 5. The results indicate that the transmission efficiency of coarse aerosols is highly sensitive to the pump flow rate. At lower flow rates, the transmission efficiency exhibits a pronounced decline, particularly under conditions of elevated horizontal wind velocity.

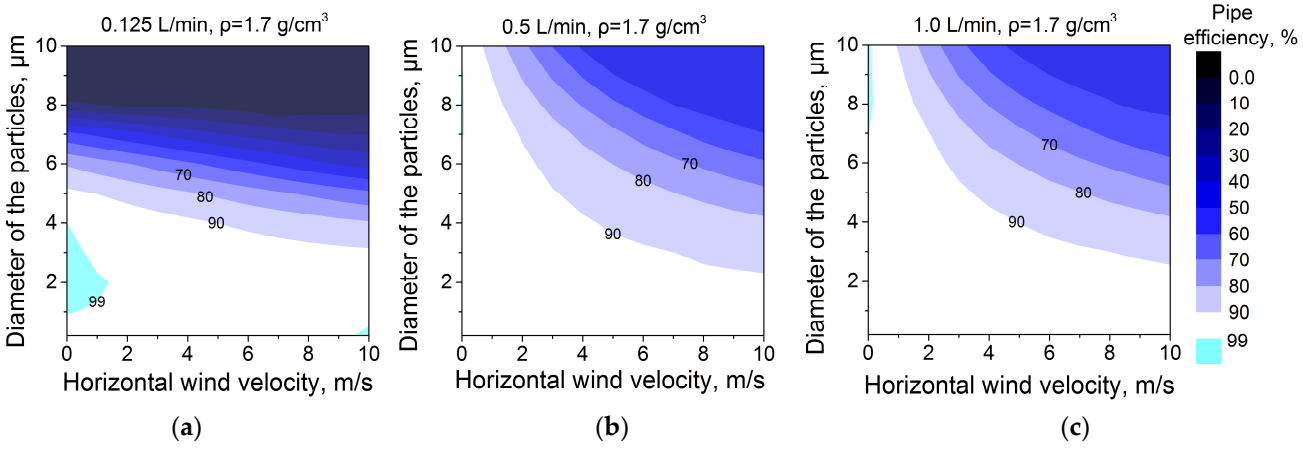

Figure 5. Transmission efficiency of the inlet pipe for eleven aerosol size fractions under varying horizontal wind velocities: (**a**) pump flow rate of 0.125 L/min; (**b**) pump flow rate of 0.5 L/min; (**c**) pump flow rate of 1.0 L/min.

The model calculations indicate that at wind speeds up to 2 m/s and pump flow rates between 0.5 and 1.0 L/min, the efficiency of the developed system ranges from 90% to 99.5% across all particle diameters. Furthermore, wind speeds up to 10 m/s have minimal impact on the sampling efficiency for particles smaller than 2.5 µm at pump flow rates of 0.125 to 1.0 L/min.

However, at a pump flow rate of 0.125 L/min, a notable limitation emerges for larger particles. Specifically, particles with diameters exceeding 7.5 µm are increasingly

difficult to capture, with only 20% successfully entering the system. This is attributed to gravitational sedimentation, which becomes the dominant factor for these heavier particles. Consequently, the limited performance of the SPS30 sensor pump restricts the entry of particles larger than 7.5 µm into the sensor, regardless of wind speed.

3.3. Comparison of PM Concentrations and Their Temporal Variability

The instruments demonstrate good alignment in terms of temporal variability, capturing consistent patterns in PM_x concentration changes over time, as shown in Figure 6.

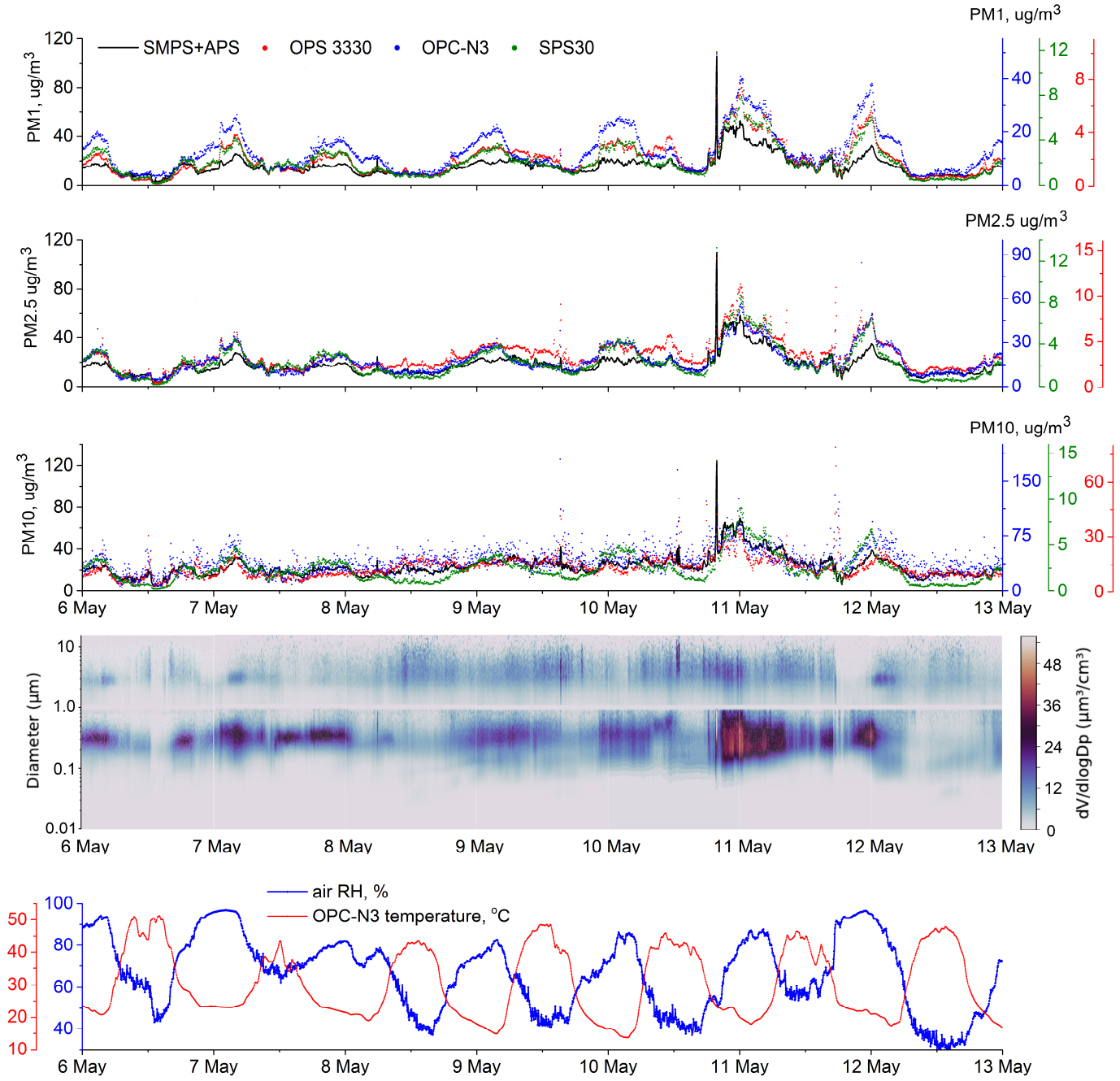

Figure 6. Series of in situ PM_x measurements by IAMU sensors; aerosol differential volume distribution $\frac{dV}{dlogD_p}$, measured by the stationary instruments SMPS 3082 and APS 3321; temperature from OPC-N3 sensor together with relative humidity (RH) data.

Data from Figure 6 show that a distinct diurnal cycle is observed in the PM_1 concentrations, which can likely be attributed to the daily evolution of the planetary boundary

layer (PBL). During daytime, convective activity within the PBL lifts near-surface aerosols, resulting in a reduction of PM_x concentrations at ground level. Following the termination of convective uplift in the evening, gravitational deposition of aerosol particles occurs, gradually increasing particle concentrations during the nighttime.

Additional factors, such as household combustion activities for evening water heating, may also contribute to elevated PM levels in the evenings due to increased low-level emissions [13]. This cyclical pattern in PM concentration dynamics provides valuable context for interpreting aerosol behavior and assessing the reliability of low-cost sensor data in capturing these temporal trends.

Large differences between absolute PM_x values were observed between the instruments, nearing one order of magnitude when optical vs. APS + SMPS benchmark PM_1 measurements are compared. However, the correlation between the time series (Table 2) remains moderate (>0.54 for PM_{10}) to high (>0.82 for $PM_{2.5}$ and PM_1) for all instruments.

Table 2. Correlation coefficient for three investigated instruments vs. reference measurements.

	SPS30	OPC-N3	OPS 3330
PM_1	0.918	0.821	0.926
$PM_{2.5}$	0.907	0.829	0.909
PM_{10}	0.676	0.546	0.679

The time series analysis and the calculated correlation coefficients indicate that the largest discrepancies occur when measuring PM_{10}. This behavior can be partially attributed to the high noise level associated with the OPC-N3 sensor. For the SPS30 and OPS 3330 sensors, however, other factors may contribute to the observed discrepancies. It is important to note that while the comparison of PM concentrations from IAMU sensors shows good correlation coefficients with reference measurements, significant discrepancies in absolute values are observed, which can exceed 100%. The next sections focus on investigating the potential factors influencing measurement discrepancies.

3.4. Measurement Results for Different Ambient RH and Instrument Temperature

The effect of relative humidity (RH) of the air sample on the results of PM concentration measurements was investigated. For this purpose, a set of simultaneous measurements made by IAMU sensors with a time step of 5 min relative to the reference instrument during a weekly measurement campaign was analyzed. Figure 7 shows the results of such measurements as a set of scatter plots, where the color of each point corresponds to one of three intervals of RH of the air sample: dry, intermediate, and humid.

The data from Figure 7 shows the division of measurements into groups depending on the RH of the air sample, which makes it possible to calculate the growth factor (GF), defined [14] as the coefficient of the increase in particle diameter due to hygroscopic growth. This comparison under different relative humidity scenarios highlights the influence of hygroscopic growth on aerosol measurements, particularly in the PM_1 and $PM_{2.5}$ ranges where particle size is more sensitive to ambient humidity.

Additionally, the impact of temperature on the measurements was examined to enhance measurement accuracy. Figure 8 shows growth factor (GF) values on RH dependencies measured by IAMU sensors together with temperature variations inside the enclosure. The relationship between GF and relative humidity (RH) was analyzed, revealing distinct patterns across the sensors. Both the OPC-N3 and OPS 3330 sensors displayed similar behavior. For RH levels below 65%, no statistically significant trend was observed. However, when RH exceeded 65%, a positive correlation emerged, though further verification is needed, particularly for the OPS 3330 PM2.5 measurements.

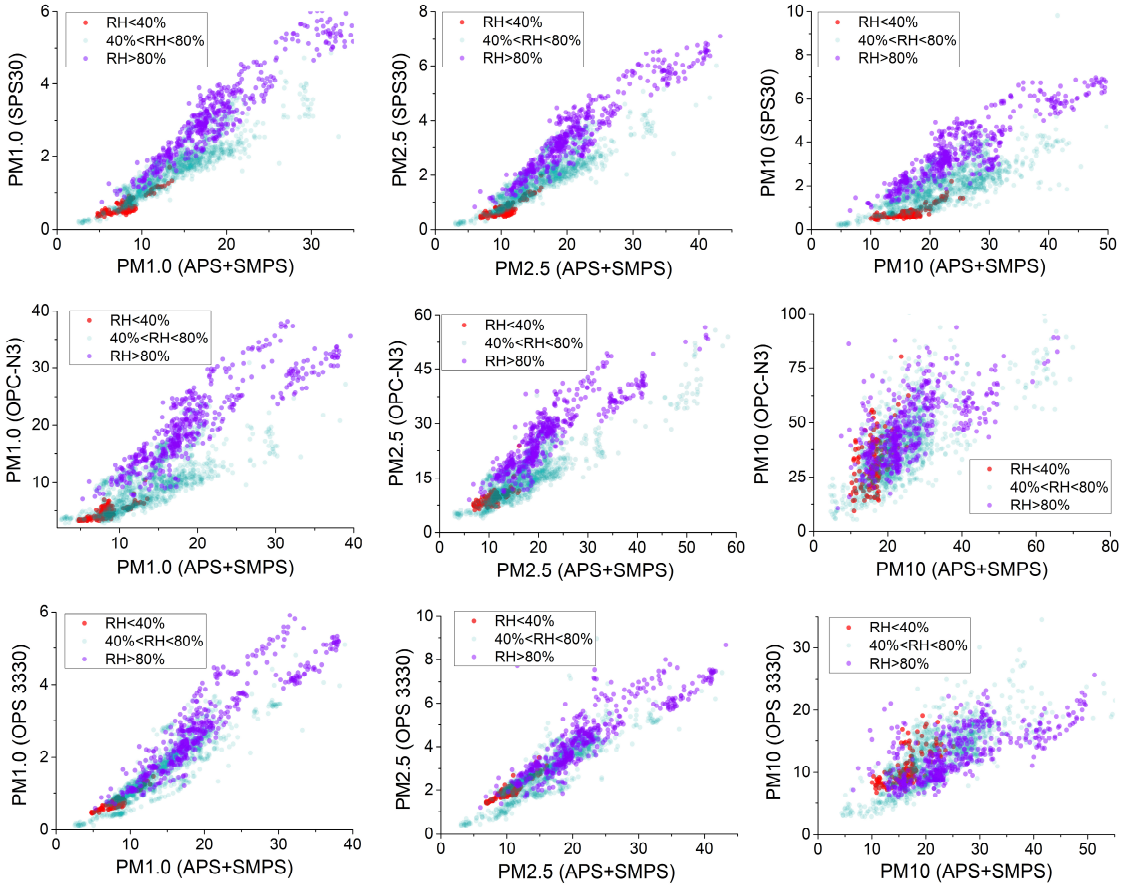

Figure 7. PM_x values measured by SPS30, OPC-N3, and OPS 3330 instruments, compared to values from reference size spectrometers (SMPS 3082 and APS 3321) for different RH values.

In contrast, PM_{10} measurements showed no significant trend across the entire RH range. Notable outliers were observed around RH ≈ 90%, which may require further investigation to determine the underlying causes. The consistent behavior between the OPC-N3 and OPS 3330 sensors suggests that similar mechanisms are driving their response to changes in RH.

Both the OPC-N3 and OPS 3330 sensors demonstrated sensitivity to hygroscopic growth, particularly for PM_1, at relative humidity levels exceeding 65%, which is in consent with optical measurements of hygroscopic effect in the laboratory conditions [15]. In contrast, the SPS30 sensor did not exhibit a similar response for PM_1, though a comparable dependence on RH was observed for larger particles with SPS30.

It should be noted that the SPS30 sensor exhibited a distinct response pattern likely influenced by its internal algorithm. A positive RH dependency was evident across all RH levels, including relatively dry conditions around 40%, with a consistent slope of this dependency across the RH spectrum. This behavior suggests the application of an RH-dependent correction factor within the SPS30's internal processing. Furthermore, the distribution of observed values for each PM_x category (PM_1, $PM_{2.5}$, and PM_{10}) varied, so the uniform distribution pattern across size ranges implies that predefined calibration constants are used. This approach limits the SPS30 sensor's ability to precisely differentiate between particle size distributions.

An analysis of the calculated GF values was carried out for the PM_1 measurement results in order to identify general patterns. Figure 9 shows linear fitting aiming to find deliquescence point (DRH). Here, the deliquescence point is assessed as the point of

transition between two fitted linear functions. Also, data points for RH values more than 90% (shown in gray color) have been excluded from the analysis.

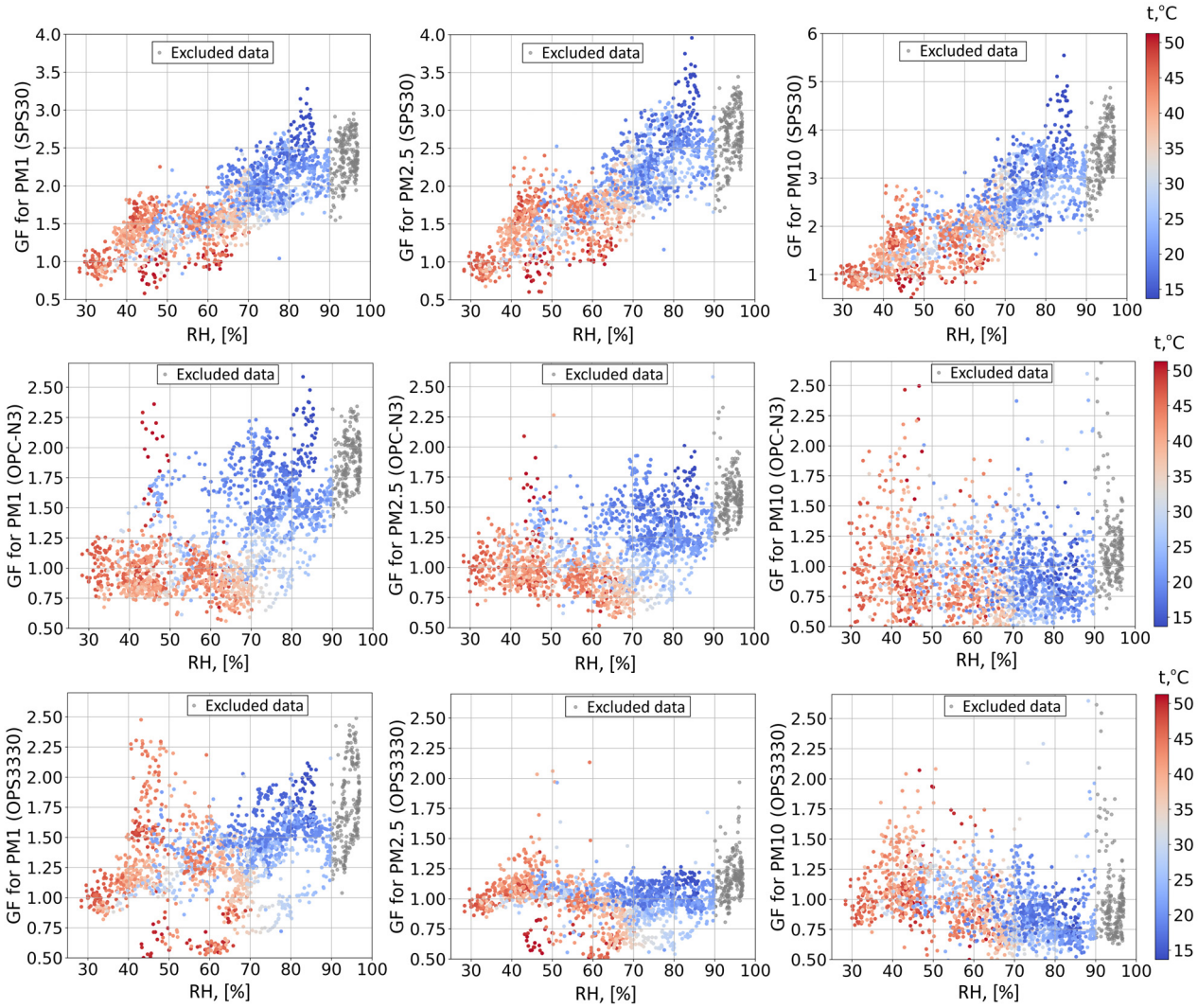

Figure 8. GF values calculated for PM_1, $PM_{2.5}$, and PM_{10}, measured by the SPS30, OPC-N3, and OPS 3330 sensors, are compared with values obtained from reference size spectrometers (SMPS 3082 and APS 3321) at different RH levels.

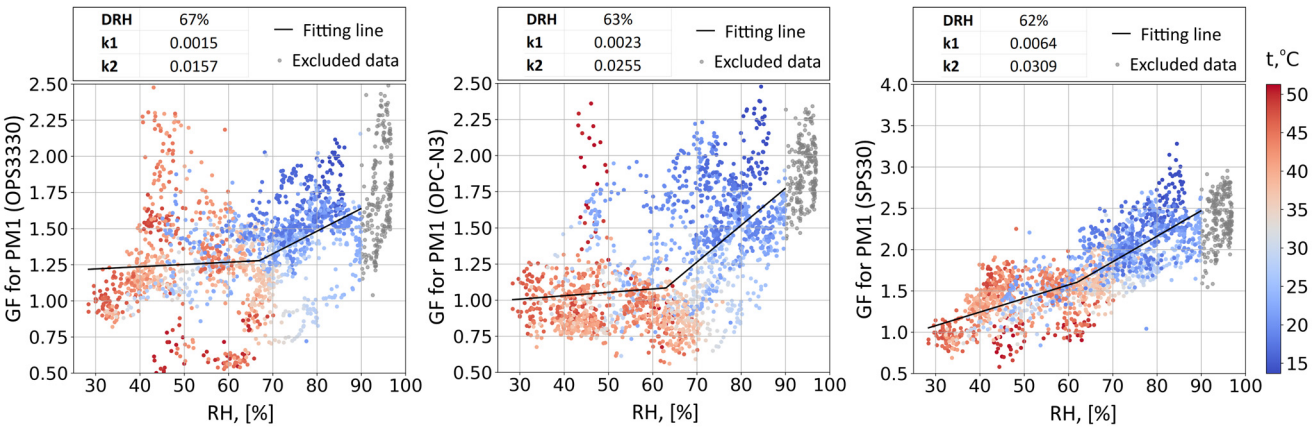

Figure 9. GF values calculated for the OPS 3330, OPC-N3, and SPS30 sensors, including bi-linear fitting and the deliquescence relative humidity point (DRH).

It should be noted that, for RH values exceeding approximately 65%, a noticeable change in the dependence of the GF on RH was identified for all IAMU sensors, particularly for PM_1 measurements. Additionally, considering that atmospheric thermodynamics suggest an inverse relationship between RH and temperature, and taking into account the temperature distribution observed in the scatter plots from Figure 8, both RH and temperature may partially contribute to the variations observed in sensor performance.

Thus, a correlation between RH and temperature could be observed, highlighting the potential influence of ambient conditions on sensor performance. To further investigate this relationship, the study explored whether the apparent temperature dependence could be attributed to a secondary effect of RH, considering the established interplay between these parameters.

3.5. Calibration Method for Different Ambient RH and Instrument Temperature

The response of measured PM data to fluctuations in RH was assessed to understand how ambient moisture impacts the measurements by each sensor. Also, it should be noted that the IAMU has a black plastic enclosure without thermal stabilization, which provides relatively big differences in the temperature of its sensors during the day. The temperature of the sensors can affect measurements, and the following method was proposed for the IAMU sensors' calibration:

1. Data from three different low- and mid-cost instruments were processed simultaneously, measuring a non-conditioned aerosol mixture, and compared to a reference instrument (APS + SMPS). The reference instrument conditioned the aerosol sample to an RH below 40%, in accordance with the recommendations of the Global Atmosphere Watch [16], which suggests that at RH levels below 40%, hygroscopic growth in aerosols is minimal, ensuring stable, dry measurements for accurate comparison.
2. From the collected data, a subset of measurements was identified that met two specific conditions: the RH of the air sample was below 40% (when hygroscopic growth can be assumed negligible), and the PM values recorded by the reference instrument were within a 5% temporal variance. This filtering step was applied to ensure the reliability of the data and to maintain consistency between the low- and mid-cost instruments and the reference system.
3. For each time point, the GFraw from the sensor to be calibrated was calculated as GFraw = PMsensor/PMref. This calculation allowed for the determination of a conversion factor, Γ, between GF and GFraw, where $\Gamma = 1/\mathrm{GFraw}$, assuming that GF = 1 when RH < 40%. Using obtained conversion factors Γ for RH < 40%, all GFraw values from three sensors were recalculated following the formula: $\mathrm{GF} = \Gamma \cdot \mathrm{GFraw}$. The resulting conversion factors Γ for each of the three sensors across all PM_x values are presented in Table 3.
4. Temperature measurements within the enclosure were taken from the OPC-N3 sensor. Since all three sensors were housed together, we assumed a uniform temperature for all three instruments. To eliminate the influence of the relative relationship between sensor temperature and ambient RH, a correlation analysis was performed to extract the independent component of the temperature data. A corrected temperature t_{corr} was introduced, defined as $t_{corr} = t - f(\mathrm{RH})$, where $f(\mathrm{RH})$ represents the linear regression function describing the relationship between sensor temperature (t) and ambient RH. This approach allowed for the assessment of the linear dependence between temperature and RH. To ensure that the analysis was focused solely on cases where RH variability could not be attributed to temperature changes, a threshold deviation of 2.5 °C was empirically selected. Cases where the temperature variability

exceeded this threshold were excluded from further analysis to ensure the robustness of the results.

5. Filtered by an empirically selected t_{corr} interval, the corresponding GF values were approximated for the RH < 90% using the following function [14,17]:

$$GF = 1 + \frac{A \cdot \kappa}{\frac{100}{RH} - 1}, \quad (10)$$

where A is the internal sensor's calibration coefficient, which may be different for SPS30 and OPC-N3.

Table 3. Conversion factors Γ between reference instrument and IAMU sensors for dry air sample.

	SPS30	OPC-N3	OPS 3330
PM_1	14.110	1.679	11.875
$PM_{2.5}$	16.308	1.176	5.434
PM_{10}	23.600	0.529	1.677

Following the proposed methodology, the GF values measured by the sensors were recalculated after filtering by temperature t_{corr}, while preserving the dependence of hygroscopic growth on RH. The recalculated GF values are presented in Figure 10, which illustrates the effects of hygroscopic growth by showing the GF ratios across all IAMU sensors as a function of RH.

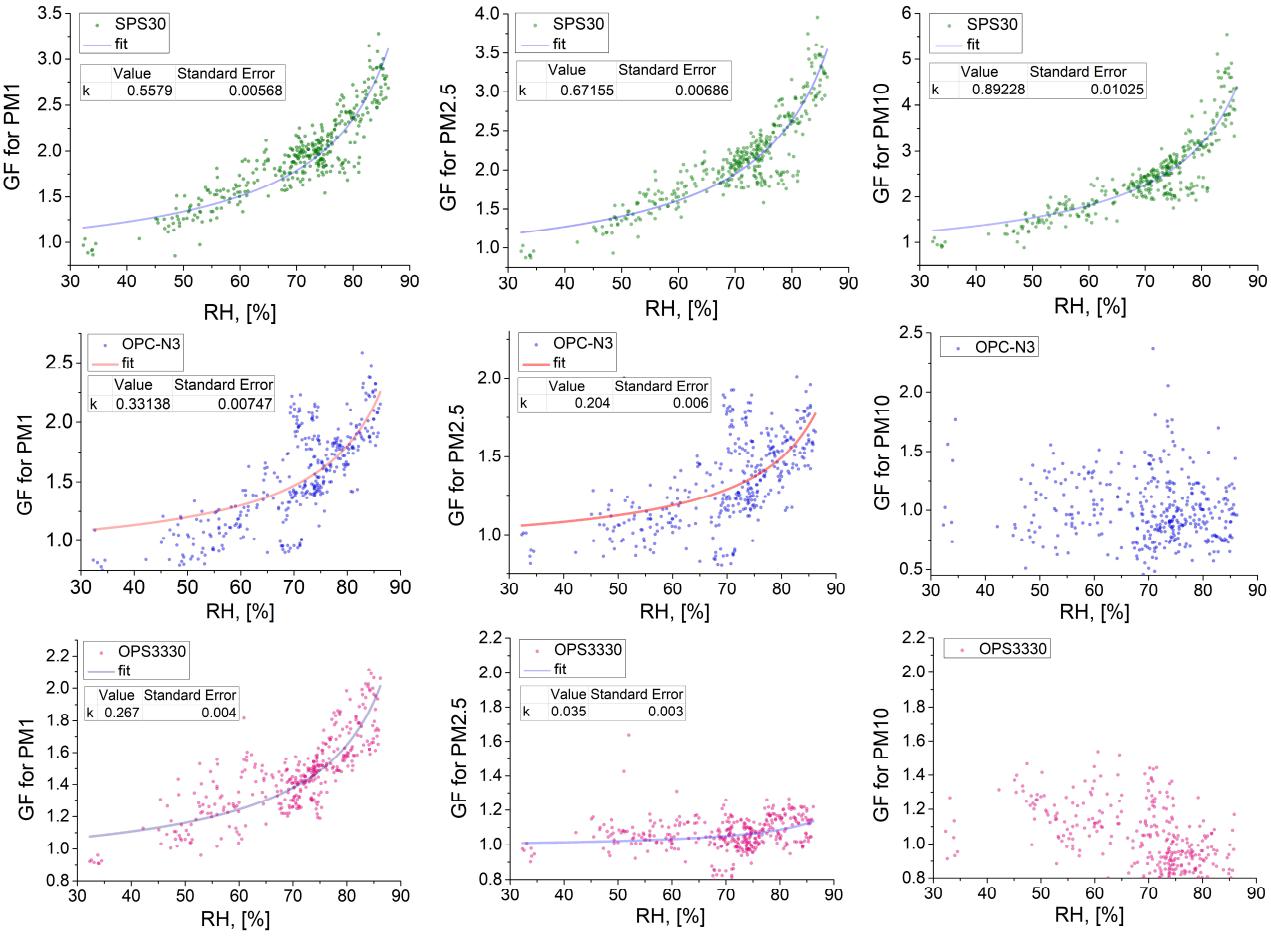

Figure 10. Comparison of GF in situ measurements for PM_1, $PM_{2.5}$, and PM_{10}, by the SPS30, OPC-N3, and OPS 3330 sensors, with values obtained from reference instruments (SMPS 3082 and APS 3321) at different RH levels. Fitting is performed according to Equation (10).

For RH values exceeding 70%, all low-cost sensors reported overestimated PM concentrations, likely reflecting the influence of particle-bound moisture. In contrast, PM_{10} measurements were generally less affected by RH variations, with the exception of the SPS30 sensor, consistent with the expected behavior of coarser, predominantly hydrophobic aerosols, such as mineral dust. These findings underscore the importance of incorporating RH conditioning or correction factors in low-cost instruments when operating in humid environments. Such measurements are critical to achieving consistency with high-accuracy systems that rely on measurements of dry aerosol samples.

However, the effects of hygroscopic growth were notable across low- and mid-cost instruments, particularly in the PM_1 and $PM_{2.5}$ size ranges. For PM_{10}, this effect was less consistent, appearing predominantly in the SPS30 measurements. Statistical analysis indicates that hygroscopic growth effects become pronounced as RH exceeds 70%, where particle-bound moisture content increases, leading to overestimation in low-cost sensors.

This hygroscopic influence is less apparent in PM_{10} due to the coarse aerosol fraction (>2.5 μm) generally being dominated by mineral dust, a largely hydrophobic aerosol type [18]. This trend aligns with findings from other studies, which show that larger mineral particles resist hygroscopic growth, unlike finer, more hydrophilic aerosols typically found in PM_1 and $PM_{2.5}$ [19]. These distinctions underline the importance of RH conditioning in accurately assessing PM measurements across different size fractions and environmental conditions.

Thus, the application of the proposed method allowed us to obtain theoretically justified dependences of GF on RH for PM_1 and $PM_{2.5}$ concentrations from noisy one-week time series data and did not affect the dependence of GF on RH for PM_{10} concentrations, which, in total, is consistent with mineral dust aerosol measurements. Also, assessments of the κ-parameters as sensor calibration parameters for PM_1 and $PM_{2.5}$ concentrations were obtained (see Figure 10).

3.6. Uncertainty Estimations of the Calibration Method

The uncertainty assessment of the PM calculation was carried out based on the ISO-Guide (ISO/IEC Guide 98-3:2008) [20], which was applied to the equation:

$$PM = PM_{raw} \cdot \Gamma = PM_{raw} \cdot \frac{PM_{Ref(\mathrm{RH<40\%})}}{PM_{Sensor(\mathrm{RH<40\%})}}, \quad (11)$$

where PM—the result of recalculation of raw values PM_{raw} from a sensor; PM_{raw}—the measurement result from a sensor that is subject to recalculation; $PM_{Sensor(\mathrm{RH<40\%})}$ and $PM_{Ref(\mathrm{RH<40\%})}$—the measurement results, made during the calibration campaign by a sensor and the reference instrument, respectively. For convenience, the following designations were introduced: $PM_S = PM_{Sensor(\mathrm{RH<40\%})}$ and $PM_R = PM_{Ref(\mathrm{RH<40\%})}$. Assuming that all quantities on the right-hand side of (11) are independent and the correction is applied to one measurement, PM_{raw}, the total standard uncertainty can be calculated by the formula [20]

$$u_{PM} = \sqrt{u^2_{PM_R} + \Gamma^2 \cdot u^2_{PM_S}} \quad (12)$$

where Γ^2—sensitivity coefficient; u_{PM_s} and u_{PM_R}—standard uncertainties of measurements by the sensor and the reference instrument, respectively, during the calibration campaign.

Considering that APS and SMPS were used to determine the reference values for PM_1, $PM_{2.5}$, and PM_{10}, the estimation of the expanded uncertainty $u_{PM_R} = 29\%$ has been used for all cases, based on [10]. The evaluated total standard uncertainties assessed from the measurement campaign data for the IAMU sensors are presented in Table 4:

Table 4. Uncertainties assessment u_{PM} for dry air sample for IAMU sensors.

	SPS30	OPC-N3	OPS 3330
PM_1	36.07%	46.10%	33.80%
$PM_{2.5}$	42.23%	35.79%	33.41%
PM_{10}	-	106.5%	71.74%

4. Discussion

Three low-cost optical aerosol sensors were evaluated against benchmark measurements that operated on dried aerosol samples, revealing moderate to strong correlations that indicate good sensitivity to the changes in the aerosol concentrations. However, we observed significant differences in the absolute PM_x values when compared with the high-performance (non-optical) instruments. Such a mismatch is not surprising, as the difficulty of calibrating optical aerosol sensors is a problem well-known in the literature [21–23]. Optical instruments can detect fine aerosols with diameters above approximately 300 nm, which means that a large fraction of the smallest aerosol particles cannot be observed using optical methods. Moreover, low-cost instruments are typically calibrated using pre-prepared aerosol samples. The commonly used monodisperse Polystyrene Latex (PSL) spheres can have optical parameters that differ significantly from ones displayed by ambient aerosol samples. Therefore, variations in aerosol density, refractive index, shape, and hygroscopic growth factor can introduce substantial systematic errors in ambient optical measurements.

Specifically, the hygroscopic growth of aerosol particles can be the leading contributor to uncertainties in low-cost instruments that do not precondition the aerosol sample before measurement. In the presented study, the response to humidity varied between sensors: all detected hygroscopic growth in the fine fraction, but the SPS30 showed consistent changes with RH across all PM fractions, suggesting either non-independent coarse measurements or internal HG corrections. In contrast, the OPC-N3 and OPS 3330 demonstrated agreement in HG influence, with a significant increase in the measured values above approximately 65% RH. Temperature effects on the sensors were corrected using a linear regression-based approach, although its validity under varying atmospheric conditions remains uncertain due to the limited time-series and stable meteorological conditions during the study. Longer, multi-seasonal data collection is needed to confirm its broader applicability.

Hygroscopic growth was quantified by fitting a theoretical function, with no HG observed for PM_{10} measured by OPC-N3 and OPS 3330, indicating hydrophobic characteristics of the coarse aerosol fraction. The study demonstrates that, in principle, conversion factor k, temperature correction filtering, and HG can be estimated for any optical low-cost sensor operating in a defined and relatively stable set of conditions. These factors can be then used to calculate true (dry) PM_x values for a given location. It is likely that if significantly different conditions were present, such a calibration would fail. Therefore, in future studies, we aim to perform similar measurements in various seasons and locations to create a Lookup table of calibration coefficients that would allow for the conversion of data from low-cost optical instruments to reasonably precise PM_x measurements.

On the other hand, the proposed calibration approach can be readily used to perform ad hoc calibrations of airborne optical instruments mounted on UAVs to perform vertical soundings of atmosphere in a vicinity of high-performance, ground-based aerosol stations. Such calibrations should yield satisfactory results, provided the type of aerosol (i.e., density, shape, and refractive index) does not change strongly with altitude within the UAV's operational altitudes.

5. Conclusions

Three low- to mid-cost optical aerosol sensors were compared and validated against state-of-the-art non-optical instruments. All sensors demonstrated satisfactory sensitivity to changing aerosol concentrations in different size fractions. However, the presented study shows the importance of calibrating low-cost optical sensors to the specific aerosol types and atmospheric conditions (mainly RH) that they operate in. The simple assumption that the manufacturer's off-the-shelf calibration can be used for all aerosol types can lead to very large errors, even exceeding one order of magnitude.

A calibration approach is formulated in the presented study to address these issues and to significantly lower the uncertainties of a low-cost optical sensor. Such a calibration is only valid if the hygroscopic characteristics of the sampled aerosols remain stable. Still, these characteristics can be approximated based on aerosol chemical models or, alternatively, by statistical analysis of aerosol composition at a given measurement location.

Author Contributions: Conceptualization, A.P., A.S. and I.B.; methodology, A.S. and I.B.; software, J.S.; validation, I.B., J.S., A.P. and A.S.; formal analysis, I.B., J.S., A.P. and A.S.; investigation, I.B., A.P. and A.S.; resources, J.W. and I.B.; data curation, I.B., A.P. and A.S.; writing—original draft preparation, I.B. and A.S.; visualization, I.B. and J.W.; supervision, A.P.; project administration, A.P.; funding acquisition, A.P. All authors have read and agreed to the published version of the manuscript.

Funding: This research was funded by the National Science Centre, Poland, grant number 2021/41/B/ST10/03660.

Institutional Review Board Statement: Not applicable.

Informed Consent Statement: Not applicable.

Data Availability Statement: All presented data are available on demand from the corresponding author. The data are not publicly available due to embargo period.

Acknowledgments: We would like to thank ACTRIS NF Racibórz for providing high-quality aerosol size distribution data.

Conflicts of Interest: The authors declare no conflicts of interest.

References

1. Ren-Jian, Z.; Kin-Fai, H.; Zhen-Xing, S. The Role of Aerosol in Climate Change, the Environment, and Human Health. *Atmos. Ocean. Sci. Lett.* **2012**, *5*, 156–161. [CrossRef]
2. Schraufnagel, D.E. The Health Effects of Ultrafine Particles. *Exp. Mol. Med.* **2020**, *52*, 311–317. [CrossRef]
3. Pope, C.A.; Dockery, D.W. Health Effects of Fine Particulate Air Pollution: Lines That Connect. *J. Air Waste Manag. Assoc.* **2006**, *56*, 709–742. [CrossRef] [PubMed]
4. Ostro, B. The Association of Air Pollution and Mortality Examining the Case for Inference. *Arch. Environ. Health* **1993**, *48*, 336–342. [CrossRef] [PubMed]
5. Zhang, B.; Zhang, B. The Effect of Aerosols to Climate Change and Society. *J. Geosci. Environ. Prot.* **2020**, *8*, 55–78. [CrossRef]
6. Boucher, O.; Randall, D.; Artaxo, P.; Bretherton, C.; Feingold, G.; Forster, P.; Kerminen, V.M.; Kondo, Y.; Liao, H.; Lohmann, U.; et al. Clouds and Aerosols. In *Climate Change 2013 the Physical Science Basis: Working Group I Contribution to the Fifth Assessment Report of the Intergovernmental Panel on Climate Change*; Cambridge University Press: Cambridge, UK, 2013; Volume 9781107057999, pp. 571–658; ISBN 9781107415324.
7. Matsson, J.E. *An Introduction to SolidWorks Flow Simulation 2014*; SDC Publications: Mission, KS, USA, 2014.
8. Li, C.; Hu, Y.; Chen, J.; Ma, Z.; Ye, X.; Yang, X.; Wang, L.; Wang, X.; Mellouki, A. Physiochemical Properties of Carbonaceous Aerosol from Agricultural Residue Burning: Density, Volatility, and Hygroscopicity. *Atmos. Environ.* **2016**, *140*, 94–105. [CrossRef]
9. Hussein, T.; Betar, A. Size-Fractionated Number and Mass Concentrations in the Urban Background Atmosphere during Spring 2014 in Amman—Jordan. *Jordan J. Phys.* **2017**, *10*, 49–58.
10. Buonanno, G.; Dell'Isola, M.; Stabile, L.; Viola, A. Uncertainty Budget of the SMPS-APS System in the Measurement of PM 1, PM2.5, and PM10. *Aerosol Sci. Technol.* **2009**, *43*, 1130–1141. [CrossRef]

11. Bau, S.; Oury, B.; Matera, V.; Simon, X. Using Particle Effective Density to Determine SMPS-Based Aerosol Mass Concentration: Application to Airborne Carbon and Titanium Nanoparticles. *J. Phys. Conf. Ser.* **2021**, *1953*, 012004. [CrossRef]
12. Wang, H.-C.; John, W. Particle Density Correction for the Aerodynamic Particle Sizer. *Aerosol Sci. Technol.* **1987**, *6*, 191–198. [CrossRef]
13. Aquilina, N.J.; Camilleri, S.F. Impact of Daily Household Activities on Indoor PM2.5 and Black Carbon Concentrations in Malta. *Build. Env.* **2022**, *207*, 108422. [CrossRef]
14. Crilley, L.R.; Shaw, M.; Pound, R.; Kramer, L.J.; Price, R.; Young, S.; Lewis, A.C.; Pope, F.D. Evaluation of a Low-Cost Optical Particle Counter (Alphasense OPC-N2) for Ambient Air Monitoring. *Atmos. Meas. Tech.* **2018**, *11*, 709–720. [CrossRef]
15. Lee, A.K.Y.; Ling, T.Y.; Chan, C.K. Understanding Hygroscopic Growth and Phase Transformation of Aerosols Using Single Particle Raman Spectroscopy in an Electrodynamic Balance. *Faraday Discuss.* **2008**, *137*, 245–263. [CrossRef]
16. Laj, P.; Bigi, A.; Rose, C.; Andrews, E.; Lund Myhre, C.; Collaud Coen, M.; Lin, Y.; Wiedensohler, A.; Schulz, M.; Ogren, J.A.; et al. A Global Analysis of Climate-Relevant Aerosol Properties Retrieved from the Network of Global Atmosphere Watch (GAW) near-Surface Observatories. *Atmos. Meas. Tech.* **2020**, *13*, 4353–4392. [CrossRef]
17. Nurowska, K.; Markowicz, K.M. Determination of Hygroscopic Aerosol Growth Based on the OPC-N3 Counter. *Atmosphere* **2023**, *15*, 61. [CrossRef]
18. Textor, C.; Schulz, M.; Guibert, S.; Kinne, S.; Balkanski, Y.; Bauer, S.; Berntsen, T.; Berglen, T.; Boucher, O.; Chin, M.; et al. Analysis and Quantification of the Diversities of Aerosol Life Cycles within AeroCom. *Atmos. Chem. Phys.* **2006**, *6*, 1777–1813. [CrossRef]
19. Chen, L.; Peng, C.; Gu, W.; Fu, H.; Jian, X.; Zhang, H.; Zhang, G.; Zhu, J.; Wang, X.; Tang, M. On Mineral Dust Aerosol Hygroscopicity. *Atmos. Chem. Phys.* **2020**, *20*, 13611–13626. [CrossRef]
20. *ISO/IEC Guide 98-3:2008*; Uncertainty of Measurement—Part 3: Guide to the Expression of Uncertainty in Measurement (GUM:1995). ISO: Geneva, Switzerland, 2008. Available online: https://www.iso.org/standard/50461.html (accessed on 16 December 2024).
21. Giordano, M.R.; Malings, C.; Pandis, S.N.; Presto, A.A.; McNeill, V.F.; Westervelt, D.M.; Beekmann, M.; Subramanian, R. From Low-Cost Sensors to High-Quality Data: A Summary of Challenges and Best Practices for Effectively Calibrating Low-Cost Particulate Matter Mass Sensors. *J. Aerosol Sci.* **2021**, *158*, 105833. [CrossRef]
22. Liu, D.; Zhang, Q.; Jiang, J.; Chen, D.R. Performance Calibration of Low-Cost and Portable Particular Matter (PM) Sensors. *J. Aerosol Sci.* **2017**, *112*, 1–10. [CrossRef]
23. Hagan, D.H.; Kroll, J.H. Assessing the Accuracy of Low-Cost Optical Particle Sensors Using a Physics-Based Approach. *Atmos. Meas. Tech.* **2020**, *13*, 6343–6355. [CrossRef] [PubMed]